A novel manifestation at optical leaky waveguide modes for sensing applications

Goddard, Nicholas J.; Gupta, Ruchi

DOI:
10.1016/j.snb.2020.127776
10.1016/j.snb.2020.127776

Document Version
Peer reviewed version

Citation for published version (Harvard):
Goddard, NJ & Gupta, R 2020, 'A novel manifestation at optical leaky waveguide modes for sensing applications', *Sensors and Actuators B: Chemical*, vol. 309, 127776. https://doi.org/10.1016/j.snb.2020.127776, https://doi.org/10.1016/j.snb.2020.127776

A Novel Manifestation at Optical Leaky Waveguide Modes for Sensing Applications

Nicholas J. Goddard, Process Instruments (UK) Ltd, March Street, Burnley, BB12 0BT, UK; Email: nick.goddard@processinstruments.net; Phone: +44 128 242 2835

Corresponding author: Ruchi Gupta, School of Chemistry, University of Birmingham, Birmingham, B15 2TT, UK; Email: r.gupta.3@bham.ac.uk; Phone: +44 121 414 6119

Abstract: We report a very simple biosensor based on the direct observation of leaky waveguide (LW) modes as exponentially decaying interference fringes in the reflectivity curve. This phenomenon was only observed when the refractive index contrast between the waveguide and sample was low (0.002-0.005) and the LW was illuminated with a range of angles of incidence simultaneously. The LW acts as a phase object in angle space, resulting in Fresnel diffraction and formation of interference fringes for each waveguide mode. We present theory, a qualitative explanation and a mathematical model governing the formation of these fringes. The binding of an analyte to recognition elements immobilised in the LW changes its refractive index and thus the angular position of the fringes, which provides the biosensing mechanism. The reported LWs comprised a film of polyacrylamide and copolymers on glass slides, and provided high sensitivity, mass manufacturability and simple instrumentation.

1. Introduction

Optical leaky waveguides (LWs) offer the following significant benefits for sensing applications: closely-coupled referencing for reliable measurements in complex samples under uncontrolled environmental conditions [1], ease of integration with electric field driven sample processing for speed and sensitivity [2], and broad wavelength range of operation for information rich data [3]. Additionally, LWs are fabricated using solution-processing methods and widely available materials for affordability. Low cost, portable optical instrumentation fabricated by 3D printing of high rigidity polymers [4] can be used to interrogate such sensors.

The simplest LW consists of a slab waveguide with refractive index intermediate between the substrate and sample. A non-total internal reflection (TIR) method is used for partial confinement of light at the waveguide/ substrate boundary making the waveguides leaky and thus allowing prism coupling. The use of a mesoporous hydrogel layer means that recognition species can be immobilised throughout the waveguide and the sample components can diffuse in, bind to recognition species and interact directly with the optical mode(s) of the waveguide, thus providing high sensitivity (up to ~120° RIU^{-1}).

LW modes (excited at specific angles of incidence, called resonance angles) are currently visualised by depositing a metal (e.g. gold or titanium) [5, 6] between the substrate and waveguide, or by immobilizing a suitable dye in the waveguide. In this case, depending on the complex refractive index of the metal and the polarisation of the incoming light, the resonance angles appear as dips or peaks in the reflectivity curves of LWs. The deposition of the metal layer increases cost by requiring vacuum deposition and makes the integration of electric fields with LWs challenging [2]. The waveguide resonances have also been visualised by immobilizing suitable dyes in the waveguide, resulting in dips in reflectivity [7-10]. The immobilization of the dye reduces the number of available binding sites, thus reducing sensitivity, and increases non-specific absorption of sample components. Alternatively, LW resonances have been visualised by making an array of strip waveguides to obtain a strong diffraction pattern only at the coupling angle [11]. The waveguide strips were fabricated using soft lithography, which required a mould prepared by etching glass using fluorosilicic acid [11]. Alternatively, photofunctionalisable hydrogels may be used for the fabrication of LW strips [12]. This approach of visualisation of resonance angles, however, has a drawback that LWs operate as a single point sensor and hence their potential for multiplexed sensing is reduced.

We report a novel approach for the direct visualisation of LW resonance angles while offering simplicity of fabrication, an all-dielectric structure, low non-specific adsorption and multiplexed analysis capabilities. Figure 1 (a) shows the instrumental setup and (b) the output observed from the sensor, showing exponentially decaying interference fringes at the resonance angles. We also present a qualitative description and a mathematical model to understand the mechanism governing this phenomenon. The low refractive index contrast, which arises from the mesoporous nature of the waveguide material, between the hydrogel waveguide and sample results in steep 2π phase changes in the reflectivity curve at resonance angles. If such a LW is illuminated with a range of angles of incidence simultaneously, which is also beneficial for real-time monitoring of shifts in resonance angle to determine the binding kinetics, the reflected wavefront will contain sharp 2π phase changes at the resonance angles. This sharp phase change effectively shifts a small portion of the outgoing light towards higher angles, resulting in the formation of exponentially decaying interference fringes. This phenomenon has so far not been observed because of the challenges involved in fabricating a few microns thick very low index mesoporous hydrogel films [8]. The fringes were also not seen using transfer matrix modelling because this assumes a plane input wavefront, and generates the output as a function of angle by using a series of discrete angle steps. The direct observation of the LW modes *via* interference fringes in the reflectivity curve underpins the feasibility of the simplest LW with high sensitivity (119.5° RIU^{-1}), which is easily fabricated by spin coating and uses simple instrumentation (LED and CMOS camera).

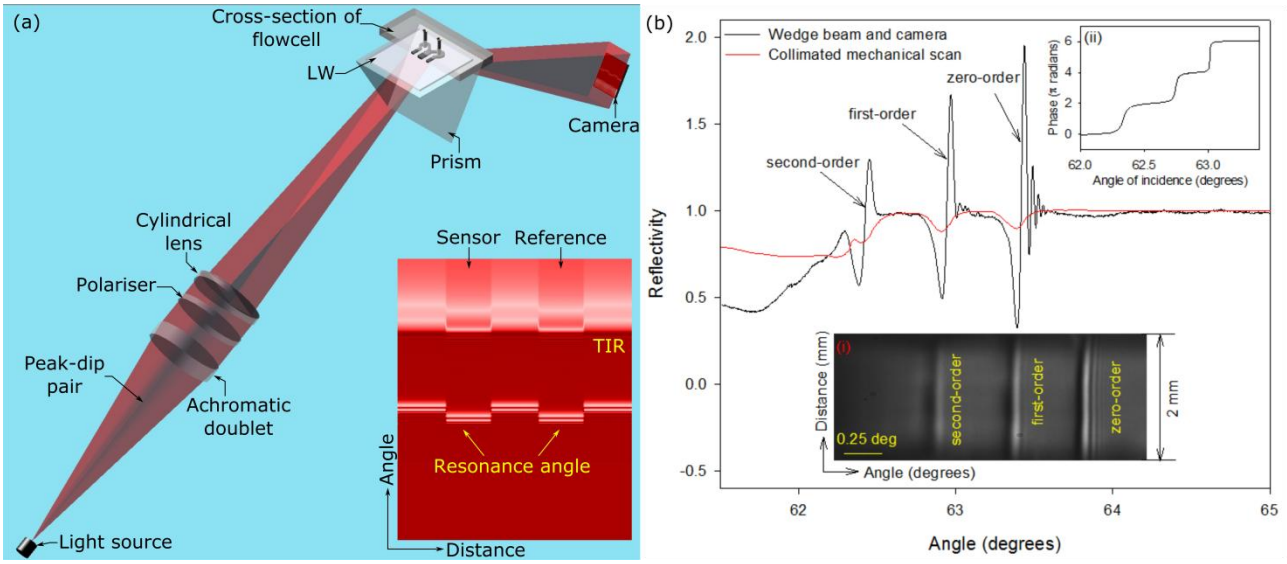

Figure 1: (a) Experimental set-up (inset shows theoretical output of a LW with low RI waveguide), and (b) experimental reflectivity curves of a LW (insets (i): LW output recorded on a camera and (ii): phase *versus* angle of incidence for a 3-moded LW based on theory)

2. Methods and Materials:

A. Chemicals and materials: 1 mm thick low iron standard microscope glass slides were purchased from VWR (Leicestershire, UK). The following items were bought from Sigma-Aldrich (Gillingham, UK): ethanol, toluene, (3-Aminopropyl)triethoxysilane (APTES), 1 M hydrochloric acid (HCl), poly(acrylamide) (poly(AAm) with M_n: 150k), poly(acrylamide-co-acrylic acid) partial sodium salt (poly(AAm-AA), M_w: 520k, M_n: 150k, acrylamide ~80%), 25% (v:v) glutaraldehyde (GA), (4-(2-hydroxyethyl)-1-piperazineethanesulfonic acid) (HEPES), 1 M sodium hydroxide (NaOH), reactive blue 4 (RB4), bovine serum albumin (BSA, A2153), biotin antibody-immunoglobulin G (anti-IgG) (B3773) and immunoglobulin G (IgG) (I5131).

Decon 90, Glycerol (M_w: 92) and N-(3-Dimethylaminopropyl)-N′-ethylcarbodiimide hydrochloride (EDC) were purchased from Fisher (Loughborough, UK). Streptavidin (N7021S, contained 140 mM, 10 mM KCl, NaCl, 8 mM sodium phosphate and 2 mM potassium phosphate) and N-Hydroxysulfosuccinimide sodium salt (sulfo-NHS) were supplied by New England Biolabs (Hertfordshire, UK) and Cambridge Biosciences (Cambridge, UK) respectively.

B. Waveguide fabrication: Glass slides were cut into squares of ~25.4 mm by 25.4 mm using a diamond scribe and cleaned in Decon 90 solution, water and ethanol for 30 mins after each step in an ultrasonic bath (Ultrawave U300H). The dried slides were treated with 1% (v:v) APTES in toluene for 30 min, washed with toluene, dried and immediately used.

The required amount of either poly(AAm) or poly(AAm-AA) was dissolved in 1 M HCl and GA was added to the polymer solution before spin coating. The concentration of GA in the polymer solution was 250 ppm. ~80 µl of the polymer solution was dispensed on a glass slide and spun for 30 s at an acceleration of 200 rpm/ s with a final spin speed between 2000 rpm and 4000 rpm. The films were allowed to crosslink overnight and then placed in deionised water to prevent further crosslinking.

C. Instrumentation: The instrumentation used to test the porosity of hydrogel films and performance of waveguide biosensors has been previously described in detail [7-9]. A simplified pictorial representation is provided in Figure 1. Briefly, a BK7 equilateral prism (Qioptic Photonics, Denbighshire, UK) was used to couple light in and out of the hydrogel waveguide. The light source (TL-6, iC-Haus, Bodenheim, Germany) and 6.6 Mpixel CMOS camera (PL-B781, Pixelink, Ottowa, Canada) were mounted on rails connected to goniometers to allow radial and angular freedom respectively. The output of the LED was collimated, transverse electric (TE)-polarised and then passed through a 40 mm focal length cylindrical lens and an aperture to form a wedge beam to probe the hydrogel waveguide with a range of angles of incidence simultaneously. The camera allowed a 7.7 mm wide section of the LW to be imaged, which allowed both the flow channels to be captured in a single frame.

The red trace in Figure 2 was obtained using a TE-polarised collimated laser (Acculase, RS Components, Northamptonshire, UK) with a peak wavelength of 650 nm and a power of 5 mW and photodiode (OSD100-6, Centronic, Surrey, UK).

Fluids were pumped through the flow cell using a peristaltic pump (Minipuls® 3, Gilson, Bedfordshire, UK) at a flow rate of 0.2 ml min^{-1}. The flowcell was CNC machined from 3 mm thick black PMMA forming two recessed cavities to obtain 2 mm wide and 0.2 mm deep channels surrounded by grooves 1 mm wide and 0.75 mm deep in which O-rings were mounted. The plate was placed on the waveguide and held in place using a water-cooled fixture maintained at 20 °C.

The refractive index of the solutions was measured using RFM900-T refractometer (Bellingham and Stanley, Kent, UK) with an accuracy of $\pm 1 \times 10^{-5}$.

D. Waveguide characterisation: The refractive index sensitivity (RIS) of the waveguides to glycerol in 100 mM HEPES buffer, pH 7.4 was tested by recording the resonance angle as glycerol solutions were pumped through the flowcell placed on the top of the waveguide. The concentration of glycerol solutions was between 0.125% (v:v) and 2% (v:v).

To study the biosensing capability of the waveguide, the poly(AAm-AA) film was activated *in-situ* by reacting the carboxylic acid groups with 1.8 mg of EDC and 2 mg of sulfo-NHS dissolved in 2 ml of 100 mM HEPES, pH 5.8 buffer re-circulated through the flowcell for ~1 h. The film was washed with HEPES buffers of pH 5.8 and then pH 7.4. The remaining solutions were prepared in 100 mM HEPES, pH 7.4. ~0.2 mg/ ml of streptavidin and BSA solutions were pumped through one channel each of the flowcell to react the amine groups in the proteins with the EDC-sulfo NHS activated poly(AAm-AA) film. The regions of the waveguide positioned under the flow channels through which streptavidin and BSA solutions were pumped provided the measurement and reference signals respectively. BSA does not bind to biotin, and hence acts as a reference channel against which the response of the streptavidin channel is measured. ~67.5 nM biotin Anti-IgG and ~133.3 nM IgG solutions were pumped through both the flow channels sequentially. A buffer wash was performed in between the protein solutions and resonance angle was monitored as different solutions were introduced on the waveguide.

3. Results and discussion

A. Direct visualisation of LW modes − Qualitative discussion

For a qualitative understanding of the formation of interference fringes at the resonance angles in the reflectivity curve of a LW, consider Figure 2, which shows a diagram of the wavefronts entering and exiting the waveguide (ignoring refraction at the prism faces), indicating the overlap between the cylindrical and plane wavefronts corresponding to the light not-coupled and coupled in the waveguide respectively. The reflected beam having cylindrical wavefronts with a 2π phase change around the resonance angle with a superimposed plane wave from the out-coupled light phase shifted by π with respect to the input phase will interfere resulting in the formation of interference fringes at the resonance angles.

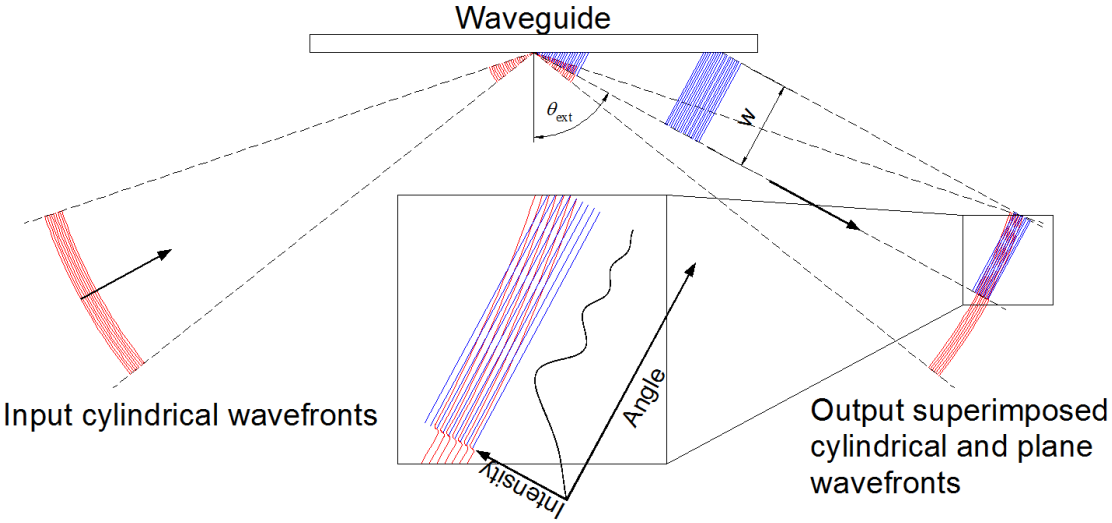

Figure 2: Wavefronts entering and exiting the waveguide, showing regions of constructive and destructive interference on exit

We observed in Figure 1 (b) that the intensity of fringes corresponding to each resonance angle decreases as the angle of incidence increases, which occurs because the plane wave exponentially decays in intensity away from the resonance angle. The intensity of the interference fringes at each resonance angle is also determined by the bandwidth of the light source used. As shown by Figure S1 in Supplementary, the interference fringes decay more rapidly for a red light emitting diode (LED) full-width half maximum, FWHM: 30 nm) than superluminescent diode (FWHM: 10 nm) and laser (FWHM: ~1 nm).

Additionally, based on Figure 1 (b), there are no interference fringes at angles lower than the resonance angle, which is because there is no plane wave at these angles. Above the resonance angle, it can be seen from Figure 2 that there is first destructive interference, leading to a dip in intensity, followed by alternating regions of constructive and destructive interference giving alternating peaks and dips in intensity. Figure 1 (b) also shows that the interference fringes were observed at resonance angles corresponding to all LW modes, but the intensity of the interference fringes decreases as the mode number increases. This is a result of the better confinement of the zero-order mode, which is observed at higher angle of incidence, in the hydrogel waveguide than first- and second-order modes because the reflectivity coefficient (R_{TE}) between the waveguide/ substrate interface increases at high angles of incidence. The angular width of the interference fringes corresponding to the zero-order LW mode was narrowest because as shown in inset (ii) in Figure 1 (b), the 2π phase change was steepest for the zero-order LW mode.

The reflectivity curve obtained by the mechanical scan of the collimated beam (red trace in Figure 1 (b)) shows the presence of dips corresponding to the resonance angles. These dips in the reflectivity curve arose because of the presence of small scattering losses in the poly (acrylamide) (poly (AAm)) waveguide. Tracking these shallow dips is difficult and results in poorer signal-to-noise ratios compared to interference fringes obtained by illuminating the LW with a range of angles of incidence simultaneously. Finally, as stated previously, this manifestation at resonance angles has so far not been observed because of the challenges involved in fabricating a few microns thick low refractive index mesoporous hydrogel films. In this work, LWs were fabricated by spin coating linear poly (AAm) solution, which was crosslinked with glutaraldehyde (GA). For example, the LW with the reflectivity curve provided in Figure 1 (b) was fabricated by spin coating 6% (w:v) solution of poly(AAm) at 4000 rpm and crosslinked *via* GA. Blocks of poly(AAm) and copolymers are commonly prepared by three-dimensional radical polymerisation of monomers and a crosslinker, bis-acrylamide. The approach is, however, not well-suited to fabricate thin films by spin coating because (1) the low viscosity monomer/ crosslinker solutions fly off without producing a thick enough film, (2) reducing oxygen inhibition of radical polymerisation in thin films is challenging, and (3) the hazardous nature of acrylamide/ bis-acrylamide. These limitations were

overcome by crosslinking of linear polymers of poly(AAm) and poly(acrylamide-co-acrylic acid) (poly(AAm-AA) with GA in acidic conditions [13], and were used in this work to fabricate the LWs.

B. Direct visualisation of LW modes − Mathematical model

The established theory of LWs is provided in the Supplementary Information, but this does not explain the appearance of the interference fringes at the resonance angles. We have developed a mathematical model to simulate the interference fringes at resonance angles in the LW reflectivity curve. A well known method based on transfer matrix approach was used[14-16] to obtain the complex amplitude transmittance coefficients of the LW at different angles of incidence for transverse electric (TE) polarized light. The transfer matrix method is based on the continuity conditions for the electric field across boundaries between adjacent layers that are derived from Maxwell's equations. From this, if the field at the beginning of a layer is known, then the field at the end of the layer can be derived by a matrix multiplication. A layer stack can be modelled using a system matrix, which is just the product of all of the layer matrices. The first and last layers are considered as semi-infinite. The reflection and transmission coefficients can be generated from the system matrix. Fresnel's approximation was then used to propagate the outgoing optical field to the detector [17-23]. MATLAB was used to obtain the shifted FFT of the amplitude transmittance coefficient, which was multiplied with equation (1).

$$H = e^{ikz} e^{-i\pi\lambda z u^2} \tag{1}$$

where, k: wave vector ($2\pi/\lambda$, m^{-1}), z: distance to the detector (m), λ: wavelength (m), u^2: quadratic phase term.

As discussed in the Supplementary Information, equation (S13), the decay length of the wave propagating in the LW (d) is a function of the "hopping length" (L) and R_{TE}, and increases as the waveguide refractive index (n_w) decreases. As shown in Figure S3 (b), Supplementary, d is ~341 µm and ~148 µm for a waveguide with RI of 1.336 and 1.38 respectively. The decay length, w, of the plane wave exiting the coupling prism is given by equation (2).

$$w = d \cos\theta_{ext} \tag{2}$$

Where θ_{ext} is the angle of incidence as defined in Figure 2. This implies that the decay length, w, of the plane wave will only be significant for waveguides of low RI. Thus, the interference between the plane and cylindrical waves is only likely to result in fringes for the waveguides of low RI.

The above mathematical model was used to obtain theoretical reflectivity curves of two LWs, where one comprised a slab waveguide of refractive index of 1.34 and other of refractive index of 1.38. The thickness of the slab waveguides was such that only the zero-order mode was supported. The wavelength was 650 nm and the propagation distance to the detector was 5 cm. As

shown in Figure 3 (a), the interference fringes were only visible when the phase change was very sharp (5 - 95% change over 0.175°), and not visible when the phase change was broader (5 - 95% change over 1.505°) for low (i.e. 1.34) and high (i.e. 1.38) RI waveguides respectively. The theoretical reflectivity profiles of 2 and 4 µm thick waveguides of RI of 1.34, which can support single and two LW modes, in Figure 3 (b) validates that the developed mathematical model can be used to explain the formation of interference fringes at all resonance angles. Additionally, based on the developed model (see Figure 3 (c)), peak-to-peak intensity increases as the distance between the prism and the camera increases.

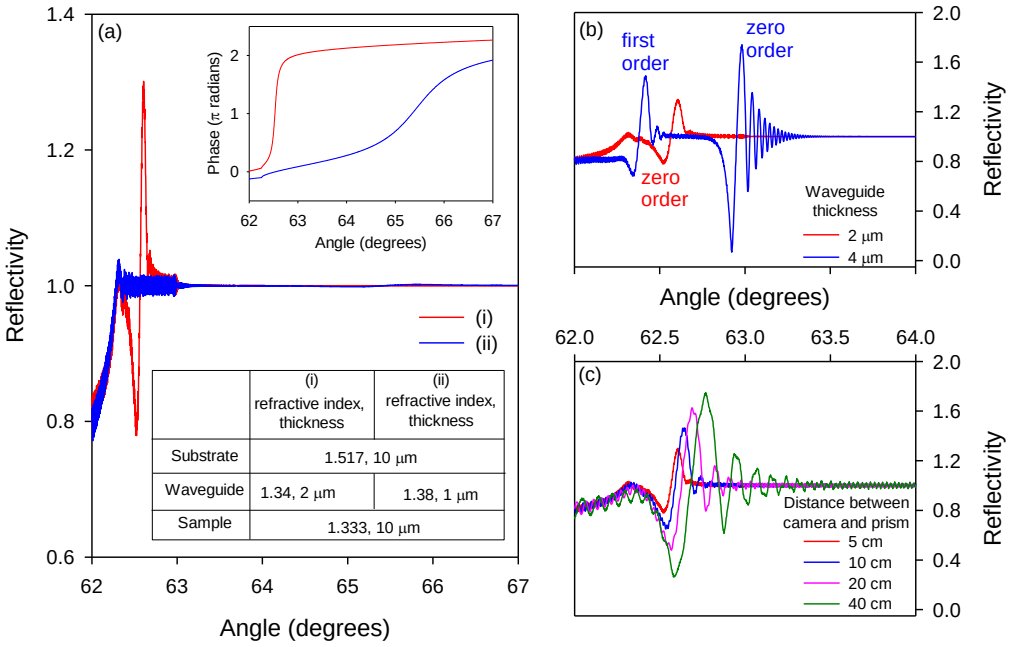

Figure 3: Theoretical reflectivity curves of LWs with waveguides of different (a) RI (inset shows their corresponding phase profiles), (b) thickness and (c) distance between prism and camera (the waveguide RI was 1.34 for (b) and (c))

C. Refractive index sensitivity (RIS)

Figure 4 shows the calculated mode profile for a 5 µm thick waveguide of refractive index 1.333667 on a BK7 substrate with a water cover layer at a wavelength of 650 nm (inset is the calculated reflectivity curve for this waveguide). It can be seen that the majority of the mode is located in the waveguide, with a small evanescent field above the waveguide. This shows that there is a strong overlap between the mode and the binding events occurring in the waveguide. In this case, the theoretical sensitivity to index change in the waveguide is 106.8° RIU^{-1}, which is 88.4% of the theoretical maximum (120.77° RIU^{-1}) for refractive index change in both the cover and waveguide layers. The theoretical RIS as a function of waveguide index is shown in Figure S4. This shows that the refractive index of the waveguide cannot be too low, or the RIS drops significantly. The choice of waveguide index is thus a compromise between RIS and the visibility of the fringes.

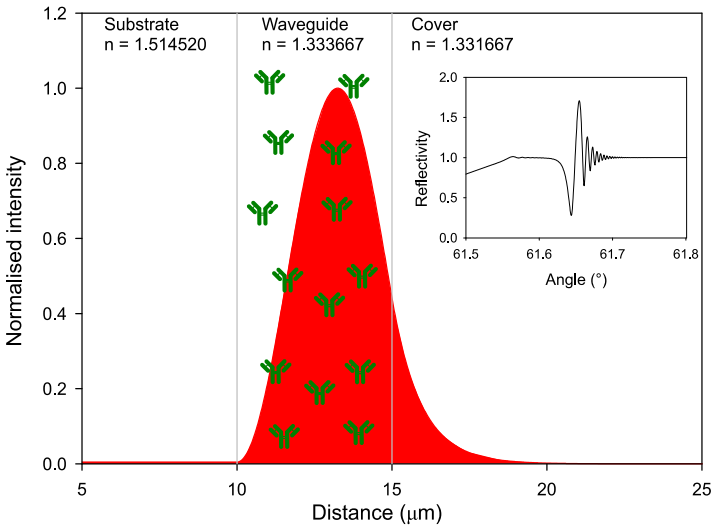

Figure 4: Mode profile of a 5 μm thick waveguide of refractive index 1.333667 at a wavelength of 650 nm, inset: theoretical reflectivity curve of the waveguide as a function of angle

The output of a single-mode LW formed by spin coating 3% (w:v) poly(AAm) is provided in Figure 5 (a). The slope of the calibration curve of shifts in the interference fringes, which represented the change in resonance angle, *versus* RI of glycerol solutions provided the RIS, which was 119.58 ± 0.37 and 119.42 ± 0.63 ° RIU^{-1} at the 95% confidence level for channels 1 and 2 respectively. This indicates that, like other refractive index biosensors, this will be linear with respect to the concentration of analyte and thus provide a quantitative measurement.

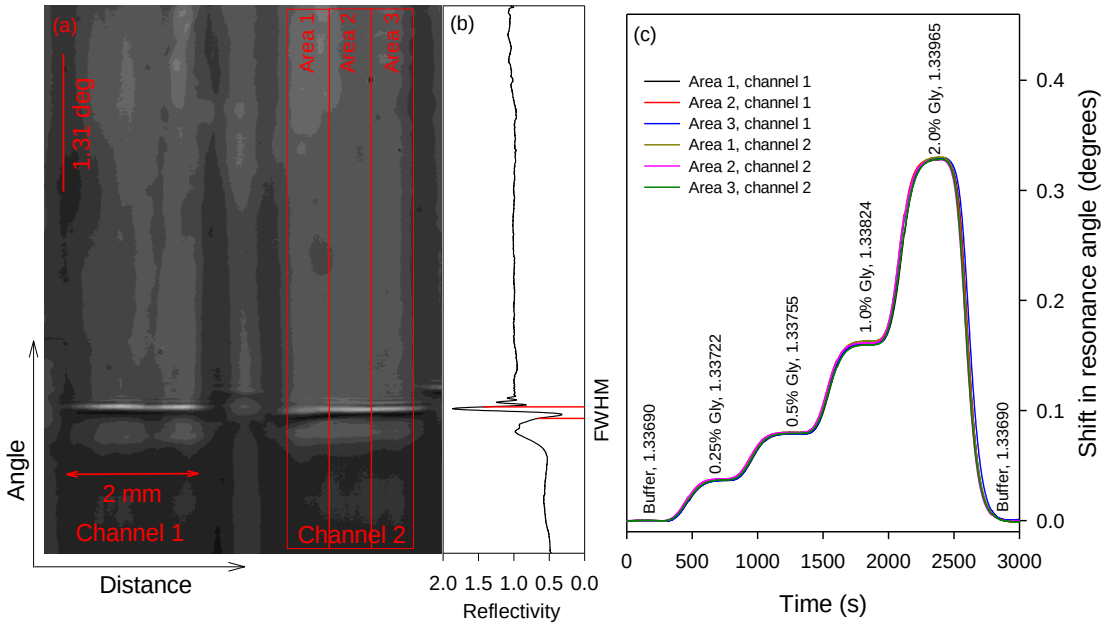

Figure 5: (a) Output of a poly(AAm) LW with a two channel flow cell mounted on top, (b) reflectivity curve showing FHWM and (c) LW response to glycerol solutions (where traces of different colours represent area-to-area variations in LW response, first three traces are for channel 1 and the last three traces are for channel 2)

A t-test on the RIS values indicates that there is no significant difference in the sensitivity of the two channels at the 95% confidence level, so the average of the two values was used (119.5 ° RIU^{-1}), which compares well with the theoretical maximum [7] of 120.97° RIU^{-1}. The figure of merit of an optical sensor is defined as the RIS divided by the FWHM of the resonance, and is how many peak widths the resonance will move for a unit change in refractive index. In this case the FWHM (from half the depth of the initial dip to half the height of the initial peak as shown in Figure 5 (b)) is ~0.106°, giving a figure of merit of ~1127 RIU^{-1}, which is considerably better (maximum 85 RIU^{-1}) than even enhanced SPR sensors [24]. The minimum detectable change in refractive index, based on three times the standard deviation of the angular noise derived from the baseline in Figure 5 (c), was 4.5×10^{-6} RIU. As shown in Table 1, the refractive index resolution determined based on signal-to-noise ratio of the baseline of LWs is comparable to commercially available SPR sensors. For practical applications, the refractive index resolution is limited by other factors such as temperature drifts and mechanical perturbations, and LW has a potential to offer improved refractive index resolution in such cases because of closely-coupled referencing [1]. Similarly, interferometers and WGM resonators have better refractive index resolution than LW, but are point-based sensors, requiring the fabrication of a separate device for each analyte. As a result, the use of these sensors for multiplexed analysis is cumbersome. In contrast, LWs can operate in imaging mode, e.g. along the width of a channel as shown in Figure 5, for multiplexed analysis.

Types of sensor	Refractive index resolution (RIU)	Benefits	Limitations
SPR with continuous metal film and prism coupling	10^{-7} to 5×10^{-6}	Well established	Expensive Requires well controlled environment
SPR optical fibre [25]	3×10^{-6} to 10^{-4}	Allows remote sensing	Less sensitive than prism coupled SPR
Mach-Zehnder/ Young interferometer [26]	10^{-8}	Internally referenced High sensitivity	Point-based sensors Phase ambiguity
Whispering gallery mode (WGM) resonators [27]	10^{-9}	High sensitivity	Point-based sensors Difficult to fabricate and use
LWs [1-3]	4.5×10^{-6}	Closely-coupled referencing	Less sensitive than interferometers and

		Broad wavelength operation Ease of integration with electric field driven sample processing Solution processed fabrication and use of affordable materials	WGM resonators

Table 1: A comparison of LW with other common label-free optical sensors where the refractive index resolution is based on signal-to-noise ratio

Figure 5 (c) also shows that the variation in the response of the LW for different glycerol solutions across both 2 mm wide flow channels was <1.55%. Minimal variations in the area-to-area response is required so that the shift in the resonance angle because of common-mode effects (e.g. temperature, composition of sample matrix) and analyte-recognition element interactions can be deconvoluted using spatially separated sensor and reference regions of the sensor.

D. Biosensing

To show that direct visualisation of LW modes is a viable option for sensing large molecules such as proteins as well as small molecules such as glycerol, sensing of an exemplar protein was performed using LWs made of poly(AAm-AA) because the hydrogel provides functional groups that allowed covalent attachment of recognition elements (e.g. antibodies) to the hydrogel waveguide. A concern was that if the waveguide index increases too much as proteins bind and displace water, the fringes would disappear, making sensing impossible. To show that this does not happen under typical usage, 3% (w:v) polymer solution containing 250 ppm GA was spin coated at 2000 rpm. The films were allowed to crosslink overnight, following which the carboxylic acid groups in the regions of the waveguide positioned under the sensor and reference flow channels were activated with EDC-sulfo NHS to allow covalent attachment of streptavidin and bovine serum albumin (BSA) respectively. Subsequently, the same solutions were pumped through both sensor and reference channels, and their corresponding response to each solution was recorded. Subtraction of the reference channel response from the sample channel response reduces the impact of common-mode effects. Figure 6 (a) shows absolute shifts in the resonance angle of the sensor and reference regions. Figure 6 (b), on the other hand, provides the differential response, which was obtained by subtracting the average response of the reference from the sensor region.

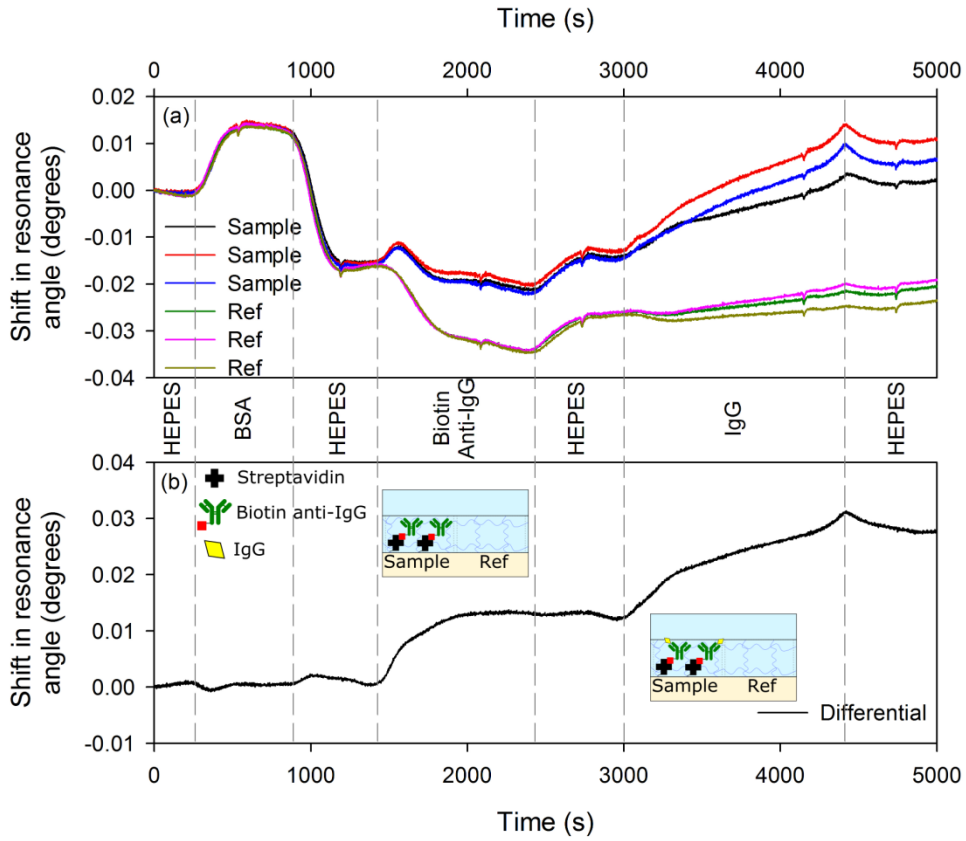

Figure 6: (a) Absolute and (b) differential response of the poly(AAm-AA) LW biosensor to different protein solutions

The shift in the resonance angle of the sensor and reference regions because of BSA was very similar and hence the differential response was negligible, showing minimal non-specific binding. Additionally, the shift in the resonance angle of the sensor and reference regions because of BSA decreased with a buffer wash. This implies that BSA was either weakly bound or unbound to ligands in the sensor and reference regions, and the shift in the resonance angle because of BSA was largely because of the refractive index different between the protein solution and buffer. A downward drift in the baseline was observed in the absolute response of the sensor and reference regions, but the baseline of the sensorgram obtained by taking a difference of the two was flat. In contrast, when biotin anti-IgG was introduced, the response in the sensor channel was much higher than the reference channel resulting in a net shift of ~0.014° in the differential trace. As biotin anti-IgG was strongly bound to streptavidin, no change in the resonance angle was observed because of the buffer wash. Similarly, IgG bound selectively to biotin anti-IgG in the sensor channel. The binding affinity between IgG and anti-IgG is lower than between streptavidin and biotin. Thus, the rate of change of resonance angle in Figure 6 (b) because of IgG-anti-IgG binding was lower than streptavidin-biotin. The small absolute angle shifts most probably arise because of the lack of a spacer, which in turn hinders reaction of the large proteins with the activated carboxylic acid groups.

5. Conclusions: We report the novel observation that leaky modes of very low index waveguides can be seen in the reflectivity curve as exponentially decaying interference fringes without any additional means of visualisation such as metal layers or dyes. This phenomenon was only observed when the waveguide was illuminated through a prism with a converging wedge beam produced by a cylindrical lens. The similarity of these fringes in reflectivity to the diffraction patterns observed when light propagates past opaque edges or phase steps led us to hypothesise, which was subsequently proved by theoretical modelling, that these patterns arose *via* a similar mechanism.

As the effective index of the waveguide layer changes, the angular position of these fringes changes, allowing binding events to be monitored in real-time. Relying solely on diffraction to visualize the waveguide resonances has resulted in a very simple optical biosensor, consisting of a glass slide with polyacrylamide and copolymers waveguide layer. The LW has a refractive index sensitivity of ~119.5° RIU^{-1}, which is comparable to the current market-leading technology, surface plasmon resonance (SPR), but has a much higher figure of merit (~1127 *versus* ~16 RIU^{-1} for unenhanced SPR). The minimum detectable change in refractive index of the LW was 4.5×10^{-6} RIU. Biosensing was demonstrated using a poly(AAm-AA) waveguide by activating the carboxylic acid groups with EDC/NHS to allow covalent immobilisation of streptavidin, followed by non-covalent binding of biotin Anti-IgG and then IgG. Future work will focus on improving the immobilisation density of antibodies in the waveguide and investigating the use of the sensor with real samples.

This work advances the field of label-free optical sensors because the reported LW may be fabricated using scalable manufacturing processes, is made of widely available low cost materials, requires affordable instrumentation, and has comparable performance to intensity-based SPR.

Acknowledgements: The authors acknowledge the funding support from the Engineering and Physical Sciences Research Council (Grants EP/N02074X/2), National Productivity Investment Fund (NPIF) and Process Instruments (UK) Ltd.

Conflicts of interest: The authors declare no conflicts of interest.

References:

[1] R. Gupta, N.J. Goddard, A novel optical biosensor with internal referencing, in: 17th International Conference on Miniaturized Systems for Chemistry and Life Sciences, Freiburg, Germany, 2013, pp. 1490-1492.

[2] N.J. Goddard, R. Gupta, Speed and sensitivity – integration of electrokinetic preconcentration with a leaky waveguide biosensor, Sensors and Actuators B - Chemical, 301 (2019) 127063-1-127063-7.
[3] R. Gupta, N. Alamrani, G.M. Greenway, N. Pamme, N.J. Goddard, A method for determining average iron content of ferritin by measuring its optical dispersion, Analytical Chemistry, 91 (2019) 7366-7372.
[4] R. Gupta, N.J. Goddard, H. Dixon, N. Toole, 3D printed instrumentation for point-of-use leaky waveguide (LW) biochemical sensor, IEEE Transactions on Instrumentation and Measurement, (2019), In press.
[5] Q.W. Zhang, Y. Wang, A. Mateescu, K. Sergelen, A. Kibrom, U. Jonas, T.X. Wei, J. Dostalek, Biosensor based on hydrogel optical waveguide spectroscopy for the detection of 17 beta-estradiol, Talanta, 104 (2013) 149-154.
[6] R. Gupta, B. Bastani, N.J. Goddard, B. Grieve, Absorption spectroscopy in microfluidic flow cells using a metal clad leaky waveguide device with a porous gel waveguide layer, Analyst, 138 (2013) 307-314.
[7] R. Gupta, N.J. Goddard, A proof-of-principle study for performing enzyme bioassays using substrates immobilized in a leaky optical waveguide, Sensors and Actuators B-Chemical, 244 (2017) 549-558.
[8] R. Gupta, N.J. Goddard, Broadband absorption spectroscopy for rapid pH measurement in small volumes using an integrated porous waveguide, Analyst, 142 (2017) 169-176.
[9] R. Gupta, N.J. Goddard, Optical waveguide for common path simultaneous refractive index and broadband absorption measurements in small volumes, Sensors and Actuators B-Chemical, 237 (2016) 1066-1075.
[10] N.A. Alamrani, G.M. Greenway, N. Pamme, N.J. Goddard, R. Gupta, A feasibility study of a leaky waveguide aptasensor for thrombin, Analyst, 144 (2019) 6048-6054.
[11] R. Gupta, N.J. Goddard, A novel leaky waveguide grating (LWG) device for evanescent wave broadband absorption spectroscopy in microfluidic flow cells, Analyst, 138 (2013) 1803-1811.
[12] A.K. Pal, E. Labella, N.J. Goddard, R. Gupta, Photofunctionalizable hydrogel for fabricating volume optical diffractive sensors, Macromolecular Chemistry and Physics, 220 (2019) 1900228.
[13] I. Dmitriev, I. Kuryndin, N. Bobrova, M. Smirnov, Swelling behavior and network characterization of hydrogels from linear polyacrylamide crosslinked with glutaraldehyde, Materials Today Communications, 4 (2015) 93-100.
[14] J. Chilwell, I. Hodgkinson, Thin-films field-transfer matrix-theory of planar multilayer waveguides and reflection from prism-loaded waveguides, Journal of the Optical Society of America a-Optics Image Science and Vision, 1 (1984) 742-753.
[15] H. Oraizi, M. Afsahi, Analysis of planar dielectric multilayers as FSS by transmission line transfer matrix method (TLTMM), Progress in Electromagnetics Research-Pier, 74 (2007) 217-240.

[16] M.C. Troparevsky, A.S. Sabau, A.R. Lupini, Z.Y. Zhang, Transfer-matrix formalism for the calculation of optical response in multilayer systems: from coherent to incoherent interference, Optics Express, 18 (2010) 24715-24721.
[17] R. Aalipour, Calculation of Fresnel diffraction from 1D phase step by discrete Fourier transform, Optics Communications, 382 (2017) 651-655.
[18] C. Aime, E. Aristidi, Y. Rabbia, The fresnel diffraction: a story of light and darkness, in: D. Mary, C. Theys, C. Aime (Eds.) New Concepts in Imaging: Optical and Statistical Models, 2013, pp. 37-58.
[19] M. Amiri, M.T. Tavassoly, Fresnel diffraction from 1D and 2D phase steps in reflection and transmission modes, Optics Communications, 272 (2007) 349-361.
[20] H.G. Kraus, Huygens-fresnel-kirchoff wave-front diffraction formulations for spherical waves and gaussian laser-beams - discussion and errata, Journal of the Optical Society of America a-Optics Image Science and Vision, 9 (1992) 1132-1134.
[21] D. Mas, J. Garcia, C. Ferreira, L.M. Bernardo, F. Marinho, Fast algorithms for free-space diffraction patterns calculation, Optics Communications, 164 (1999) 233-245.
[22] T. Shimobaba, N. Masuda, T. Ito, Arbitrary shape surface Fresnel Diffraction, Optics Express, 20 (2012) 9335-9340.
[23] L.Z. Cai, Q. Liu, X.L. Yang, Generalized phase-shifting interferometry with arbitrary unknown phase steps for diffraction objects, Optics Letters, 29 (2004) 183-185.
[24] Q.-Q. Meng, X. Zhao, C.-Y. Lin, S.-J. Chen, Y.-C. Ding, Z.-Y. Chen, Figure of merit enhancement of a surface plasmon resonance sensor using a low-refractive-index porous silica film, Sensors, 17 (2017) 1846-1-1846-11.
[25] B.A. Prabowo, A. Purwidyantri, K.C. Liu, Surface plasmon resonance optical sensor: a review on light source technology, Biosensors-Basel, 8 (2018).
[26] E. Makarona, P. Petrou, S. Kakabakos, K. Misiakos, I. Raptis, Point-of-Need bioanalytics based on planar optical interferometry, Biotechnology Advances, 34 (2016) 209-233.
[27] Y.N. Zhang, T.M. Zhou, B. Han, A.Z. Zhang, Y. Zhao, Optical bio-chemical sensors based on whispering gallery mode resonators, Nanoscale, 10 (2018) 13832-13856.